

First measurement of decimeter-sized rocky material in the Oort cloud

Denis Vida (✉ denis.vida@gmail.com)

University of Western Ontario <https://orcid.org/0000-0003-4166-8704>

Peter Brown

Dept of Physics & Astronomy

Hadrien Devillepoix

Space Science and Technology Centre, Curtin University <https://orcid.org/0000-0001-9226-1870>

Paul Wiegert

The University of Western Ontario <https://orcid.org/0000-0002-1914-5352>

Danielle Moser

MITS/Dynetics Technical Services

Pavol Matlovič

Faculty of Mathematics, Physics and Informatics, Comenius University

Christopher Herd

University of Alberta <https://orcid.org/0000-0001-5210-4002>

Patrick Hill

Department of Earth and Atmospheric Sciences, University of Alberta

Juraj Tóth

Faculty of Mathematics, Physics and Informatics, Comenius University

William Cooke

Meteoroid Environments Office

Donald Hladiuk

RASC Calgary Centre

Research Article

Keywords: asteroidal material, Solar System formation models, long-period comets

Posted Date: October 11th, 2021

DOI: <https://doi.org/10.21203/rs.3.rs-592064/v1>

License:   This work is licensed under a Creative Commons Attribution 4.0 International License.

[Read Full License](#)

First measurement of decimeter-sized rocky material in the Oort cloud

Denis Vida^{1,*}, Peter G. Brown¹, Hadrien Devillepoix², Paul Wiegert¹, Danielle E. Moser³, Pavol Matlovič⁴, Christopher D. K. Herd⁵, Patrick J. A. Hill⁵, Juraj Tóth⁴, William J. Cooke⁶, and Donald W. Hladiuk⁷

¹Department of Physics and Astronomy, University of Western Ontario, London, Ontario, N6A 3K7, Canada, email address: dvida@uwo.ca

²Space Science and Technology Centre, Curtin University, GPO Box U1987, Perth, WA 6845, Australia

³Jacobs ESSCA Group, NASA Marshall Space Flight Center, Huntsville, AL 35812, USA

⁴Faculty of Mathematics, Physics and Informatics, Comenius University, Bratislava, Slovakia

⁵Department of Earth and Atmospheric Sciences, University of Alberta, Edmonton, Alberta T6G 2E3, Canada

⁶NASA MEO, NASA Marshall Space Flight Center, Huntsville, AL 35812, USA

⁷RASC Calgary Centre, Calgary, Alberta, Canada

*Corresponding author: dvida@uwo.ca

1 Abstract

2 The Oort cloud is thought to be a reservoir of icy planetesimals and a source of long-period comets (LPCs)
3 implanted from the outer Solar System during the time of giant planet formation. The presence of rocky
4 ice-free bodies is much harder to explain. The rocky fraction in the Oort cloud is a key diagnostic of Solar
5 System formation models as this ratio can distinguish between “massive” and “depleted” proto-asteroid belt
6 scenarios and thus disentangle competing planet formation models. Objects of asteroidal appearance have
7 been telescopically observed on LPC orbits, but from reflectance spectra alone it is uncertain whether they are
8 asteroids or extinct comets. Here we report a first direct observation of a decimeter-sized rocky meteoroid

9 on a retrograde LPC orbit ($e \approx 1.0$, $i = 121^\circ$). The ~ 2 kg object entered the atmosphere at 62 km/s.
10 The associated fireball terminated at 46.5 km, 40 km deeper than cometary objects of similar mass and
11 speed. During its flight, it experienced dynamic pressures of several MPa, comparable to meteorite-dropping
12 fireballs. In contrast, cometary material measured by Rosetta have compressive strengths of ~ 1 kPa. The
13 earliest fragmentation of this fireball occurred at > 100 kPa, indicating it had a minimum global strength well
14 in excess of cometary. A numerical ablation model produces bulk density and ablation properties consistent
15 with asteroidal meteoroids. We estimate the flux of rocky objects impacting Earth from the Oort cloud to
16 be 0.7×10^6 km² per year to a mass limit of 10 g. This is $\sim 6\%$ of the total flux of fireballs on LPC-orbits
17 to these masses. Our results suggests there is a high fraction of asteroidal material in the Oort cloud at small
18 sizes and gives support to migration-based dynamical models of the formation of the Solar System which
19 predict that significant rocky material is implanted in the Oort cloud, a result not explained by traditional
20 Solar System formation models.

21 Introduction

22 The sharp increase in the number of ground-based networks utilizing digital cameras for observing fireballs
23 [1, 2, 3, 4, 5] in recent years has resulted in near continuous coverage of almost 2% of the Earth’s atmosphere
24 for small impactors. Supplementing these ground-based instruments in fireball detection is the Geostationary
25 Lightning Mapper (GLM) instrument on board the GOES-16 and 17 satellites. First deployed in 2016, GLM
26 now observes a total of $\sim 1/3$ of the Earth’s surface with a resolution of ~ 10 km at 500 frames per second in
27 a narrow 1.1 nm pass band centered around the O I oxygen triplet at 777.4 nm [6]. GLM is very efficient at
28 detecting bright fireballs which usually saturate ground-based cameras [7]. As camera saturation prevents an
29 accurate estimate of meteoroid properties during atmospheric entry, GLM extends the usable measurement
30 size range of bolides compared to ground-based cameras. The larger ground-based camera coverage, which
31 provides observations of fireball trajectories and orbits when fused with space-based light curves, records
32 larger numbers of the decimeter-sized meteoroid population than previously possible and allows accurate
33 estimates of their physical properties.

34 Observations from earlier fireball networks [8, 9] have established that decimeter-sized chondritic-like
35 meteoroids which penetrate deeper into the atmosphere predominantly come from asteroidal low-inclination
36 orbits, as expected. Similarly, most friable meteoroids which disrupt high in the atmosphere were measured
37 to be on Jupiter-family comet (JFC), Halley-type comet (HTC), or long-period comet (LPC) orbits. Mi-
38 nor cross-contamination of material between asteroidal and JFC orbits is observed and can explained by
39 their dynamical evolution [10], consistent with telescopic observations of comets and asteroids [11]. In-situ
40 measurements have found rocky (refractory) materials in comets [12], but these are small, microscopic chon-
41 drules and CAI fragments, presumed to be embedded during comet formation. However, the presence of
42 macroscopic (dm-sized) rocky material on nearly-isotropic comet orbits (HTC and LPC, i.e. of Oort cloud
43 origin) is much harder to explain. The abundance in the Oort cloud of larger, refractory material which
44 likely formed in the inner Solar System would be a key diagnostic in distinguishing between early dynamical
45 models of Solar System formation [13, 14, 15].

46 Contemporary models predict that a significant number of rocky objects can only be implanted in the
47 Oort cloud during a dynamical instability episode caused by the radial migration of the giant planets early
48 in Solar System history. The dynamical instability causes removal of 50 – 90% of rocky material in what
49 is now the asteroid belt in such a way as to reproduce the main-belt’s observed orbital and compositional
50 distribution [16]. These migration models necessitate a “massive” proto-asteroid belt scenario and predict
51 the ratio of icy to rocky planetesimals in the Oort cloud between 200:1 and 2000:1 [13, 17, 14, 15, 18].
52 Following this early and fast migration, a slower dynamical diffusion process is postulated to further remove
53 $\sim 70\%$ of the main-belt leaving the mass we see today [19, 20]. Recent studies show that to match the
54 dynamical and geochemical evidence, the instability occurs as early as 30 – 60 Myr after the dissipation of

55 gas in the protoplanetary disk [21, 22, 23].

56 The competing model of early Solar System formation, the pebble-accretion model, eschews the migration
57 scenario but allows for the rapid formation of the giant planets before the solar gas nebula dissipates [24].
58 In the pebble-accretion model, filaments of mm to cm-sized pebbles gravitationally collapse quickly to form
59 planetesimals [25]. The planetesimals in the terrestrial region grow more efficiently than those beyond 1
60 au, so there there is no requirement to scatter rocky material to explain the small masses of Mars and the
61 asteroid belt [26]. As the initial mass of the proto-asteroid belt is assumed to be small, the pebble-accretion
62 model predicts that virtually no scattered rocky objects are implanted into the Oort cloud. It predicts an
63 icy/rocky ratio of at most 1:10,000 [15].

64 Recently, it has been shown that the migration-induced dynamical instability is compatible with an en-
65 hanced version of the pebble accretion model which uses realistic opacities [27]. In this model, the terrestrial
66 planets form fast in only ~ 10 Myr, and then planet migration is invoked as one of the possibilities to explain
67 the hafnium-tungsten anomaly in the Earth’s mantle caused by the Theia impact [28]. Nevertheless, even
68 though the 1.5 to 4 au region is assumed to be a divergence zone, protoplanets in the zone only slowly
69 dissipate into neighbouring regions and are not scattered into highly excited orbits.

70 The earliest evidence of macroscopic asteroidal material in the Oort cloud was the discovery of asteroid
71 1996 PW [13]. Despite its highly eccentric orbit ($e = 0.997$, $i = 29.8$, and period $p = 5900$ yr), it showed no
72 cometary-like activity. It had a D-type reflectance spectrum [29], similar to bare cometary nuclei observed
73 at large solar distances and hence it’s origin as asteroid or an extinct cometary nucleus was uncertain. More
74 such objects have since been discovered with some having S-type reflectance spectra and showing activity
75 [15], further confusing the picture.

76 Pan-STARRS1 observations of LPCs have found that there is a deficit of objects with diameters $D \lesssim 1$
77 km [30], assuming the physical processes of cometary activity are size-independent. These data show a
78 significant change in the cumulative size-frequency distribution (SFD), where $N_{cum} \propto D^{-\alpha}$, for $D \sim 2.8$ km,
79 with $\alpha = 0.72$ for larger, and $\alpha = 0.1$ for smaller objects, consistent with comet formation models [31]. Thus
80 if small cometary objects existed, Pan-STARRS1 would be able to detect them. This either means that the
81 small objects are devoid of volatiles or they do not exist. Further analysis [32] has shown that $\sim 1/3$ of all
82 objects on LPC orbits detected by Pan-STARRS1 do not show any activity (called tailless “Manx” objects),
83 a surprising result considering the massive decrease in visibility of non-active bodies.

84 As telescopic measurements of an object in an LPC orbit may be compromised by space weathering
85 [33, 34], a more direct way to probe bulk physical properties of LPC material is desirable. One alternate
86 method is to observe fireballs associated with an LPC-type meteoroid entering the atmosphere [35, 36].
87 Nevertheless, such observations suffer from small atmospheric collection areas, so detection of decimeter-
88 sized objects on long-period comet orbits is rare [37].

89 By using the observed light curves and dynamics of mm and cm-sized cometary meteoroids, their ab-
90 lation behaviour is well explained if they are modelled as a collection of 10 – 300 μm sized silicate grains
91 [38]. The grain size distribution derived from observations of cometary meteoroids matches well to in-
92 situ measurements of the comet 67P/Churyumov–Gerasimenko [39, 40]. Similarly, observations of dm-sized
93 meteorite-dropping fireballs can be well explained by modelling them as rocky objects which fragment deep
94 in the atmosphere when aerodynamic loading exceeds their global mechanical strength [41]. In most cases,
95 global strengths of meteorite-producing fireballs are found to be much lower than the compressive strengths
96 of their associated meteorites, a finding ascribed to internal cracks [36].

97 From decades of observations, it is now well established that there is a strong correlation between me-
98 teoroid material type and bulk strength [42]. Cometary meteoroids are weak and disrupt under dynamic
99 pressures of ~ 1 kPa [43] upon entering the atmosphere, while asteroidal meteoroids can withstand pressures
100 of 100 kPa prior to any fragmentation [36], with their strongest components withstanding pressures of up to
101 1 – 10 MPa without catastrophic disruption [44]. These differing strengths explain why cometary fireballs
102 break up at heights above 70 km [1], while meteorite dropping fireballs break up typically below 40 km [36].
103 For cometary meteoroids, the strength of constituent 10 – 300 μm silicate grains is on the order of 10s of
104 MPa [45], but high porosity significantly reduces the strength of larger grain aggregates [46].

105 In-situ measurement of the nucleus of comet 67P by the Philae lander found a surface compressive
106 strength of 1 – 3 kPa [47], a value consistent with in-atmosphere measurements of cometary meteoroid
107 strength [48]. The probe stopped bouncing when it hit an area of crushing strength > 4 MPa, possibly
108 a processed, tightly packed “sintered” surface layer [49]. Despite having a high compression strength, the
109 surface layer was also found to have a high porosity of 30 to 65% [50], thus limiting the upper bulk density
110 of the layer to 1600 – 2500 kg m^{-3} assuming an all-silicate surface. In reality the bulk density is likely
111 even lower due to the presence of ices and organic material [51]. Static penetration resistances between 6.5
112 and 10 MPa can be expected if the surface was exclusively composed of sintered CO_2 or H_2O granular ice
113 at 220 K with porosities of 50 to 70% [52]. For all of the foregoing, macroscopic samples of the surface
114 layer are expected to have smaller bulk densities than monolithic silicate material. Nevertheless, cometary
115 material might have mm-sized inclusions of stronger material. For example, some mm-sized components of
116 Taurid meteoroids (from 2P/Encke) were found to withstand pressures of up to 300 kPa [53, 54], and strong
117 mm-sized inclusions have been found in Leonid meteoroids (from 55P/Tempel-Tuttle)[55].

118 Categorizing meteoroid strength relies on a relative comparison of ablation behaviour. It has been shown
119 that by normalizing to meteor speed, entry angle and initial mass, the final luminous height of a fireball can be
120 used to robustly discriminate among meteoroid materials. The PE criterion [35] reduces the interdependence
121 of these measured values for fireballs into one number (see section 0.8). Meteoroids can be sorted into several
122 groups based on material properties. Type I fireballs having $\text{PE} > -4.6$ are chondritic, Type II with $-5.25 \leq$

123 PE ≤ -4.6 are related to carbonaceous chondrites, while Type III with PE < -5.25 are cometary.

124 The first reported observation of a multi-cm sized rocky meteoroid on an HTC orbit was recorded in 1997
125 over the Czech Republic, called Karlštejn [56, 57]. The ~ 200 gram object was on a retrograde orbit ($a = 3.5$
126 au, $i = 138^\circ$, $e = 0.7$, $T_J = 0.62$). It entered the atmosphere at 65 km s^{-1} and penetrated down to an end
127 height of 65 km, about 25 km deeper than cometary objects of similar speed and mass. It was classified
128 as a Type I fireball based on its PE value. Its spectrum was highly depleted in volatile elements, notably
129 sodium, and distinct from cometary fireballs. It reached a maximum dynamic pressure ($P_{\text{dyn}} = v^2 \rho_{\text{air}}$) of
130 660 kPa before ablating away gradually, indicating that the true mechanical strength of the body was not
131 reached as there was no evidence of catastrophic disruption. The dynamics of the body were consistent with
132 a chondritic density of 3700 kg m^{-3} . Nevertheless, the semi-major axis was smaller than most long-period
133 comets and the dynamic pressures lower than what decimeter-sized chondritic meteorite-dropping fireballs
134 withstand due to the small mass of the body. The authors theorized it was a cm-sized rocky component
135 originally embedded in a comet[56].

136 Records from decades of meteor shower observations have not revealed any macroscopic ($> \text{cm}$ -sized) lithic
137 material mixed in with fragile HTC or LPC cometary meteoroids. Smaller inclusions have been documented,
138 notably several mm-sized Type I fragments of Leonid fireballs were observed during the 1998 Leonid fireball
139 storm [55, 58, 59] as have some gram-sized Type I Taurids [1]. However, the Taurids are an unusual stream;
140 they are on the dynamical boundary between JFC and asteroidal orbits, are generally classified as Type
141 II material, can be difficult to separate from the sporadic background and have an origin likely related to
142 fragmentation rather than gas drag sublimation [54].

143 Most recently, a survey [39] of mm-sized meteoroids which analyzed their spectral and fragmentation
144 properties, identified two iron meteoroids on HTC orbits (out of a total of 64 HTC meteors). The authors
145 suggested these were ejected during the formation of the Solar Solar due to the dynamical instability caused
146 by Jupiter's migration.

Table 1: Geocentric radiant and heliocentric orbit (J2000.0). For the orbital covariance matrix, see Table 7 in Methods.

Description		Value	1σ error
Geocentric right ascension of radiant	α_g	271.922°	$\pm 0.038^\circ$
Geocentric declination of radiant	δ_g	4.40°	$\pm 0.14^\circ$
Geocentric entry speed (km s ⁻¹)	v_g	60.97	± 0.03
Semimajor axis (au)	a	104	± 53
Eccentricity	e	0.9941	± 0.0027
Perihelion distance (au)	q	0.6150	± 0.0015
Argument of perihelion	ω	103.95°	$\pm 0.23^\circ$
Longitude of ascending node	Ω	333.857472°	
Inclination	i	121.40°	$\pm 0.24^\circ$
Aphelion distance (au)	Q	207.2	± 105.4
Last perihelion date		2021-01-16.23	± 0.08 d
Tisserand parameter w.r.t. Jupiter	T_J	-0.46	± 0.02

Table 2: Fireball trajectory parameters.

	Latitude (+N)	Longitude (+E)	Height (km, WGS84)	Time (UTC)
Begin point	53.7732° \pm 0.0009°	-112.0861° \pm 0.0005°	130.819 \pm 0.094	2021-02-22 13:23:17.683
End point	54.6182° \pm 0.0023°	-113.2543° \pm 0.0008°	46.498 \pm 0.081	2021-02-22 13:23:20.101

Results

Here we report the first direct observation of a decimeter-sized rocky meteoroid (PE = -4.49, Type I) on a long-period comet orbit ($i = 121^\circ$, $e \approx 1.0$, $T_J = -0.46$, see Table 1). This meteoroid reached dynamic pressures similar to those of ordinary chondrites. The ~ 2 kg body entered the atmosphere ~ 100 km north of Edmonton, Alberta, Canada on February 22, 2021 at 13:23:17 UTC. Its full atmospheric luminous path was recorded by two Global Fireball Observatory (GFO) all-sky cameras [3] (see Figure 1) and over 200 security and dash cameras. In addition, it was seen by both GLM systems, permitting measurement of its unsaturated light curve (see section 0.5 in Methods for GLM photometric calibration details). We used the most recent astrometric calibration methods [5] and computed the atmospheric trajectory (internal accuracy of 30 m) using the GFO data and using one additional security camera (accuracy 70 m) (see section 0.1). The fireball entered the atmosphere with a velocity of 62.1 km s⁻¹ and penetrated down to a height of 46.5 km, about 20 km deeper than the Karlštejn event of similar velocity. Table 2 lists trajectory details. The parent body search did not return any hits.

The dynamics, the light curve, and the fragmentation behaviour were modelled using a semi-empirical meteoroid ablation model [41] (see section 0.6) which has been successfully applied to multiple meteorite-producing fireballs. The comparison between observations and the model fit is shown in Figure 2, and the modelling details are given in the Methods section 0.7. A bulk density of $\rho_m = 3300$ kg m⁻³, as appropriate for chondritic meteorite-dropping fireballs [9], fits the observed dynamics well.



Figure 1: The fireball as seen from the two GFO stations (at the same scale). Top: Miquelon Lake. Bottom: Vermilion (the Big Dipper can be seen at the left side of the inset). The fireball is moving left to right, and the periodic breaks in the fireball are used to encode the absolute time.

165 As a demonstration of how improbable that this was a weak, cometary-like body, we modelled a non-
 166 fragmenting fireball using physical properties appropriate for cometary meteoroids ($\sigma = 0.08 \text{ s}^2 \text{ km}^{-2}$, $\rho_m =$
 167 1000 kg m^{-3} , τ for Type III bodies [43, 60]), with a 10 times larger pre-atmospheric mass (20 kg), and the
 168 same trajectory parameters as for our fireball. The hypothetical cometary meteoroid only penetrated down
 169 to a height of $\sim 60 \text{ km}$.

170 The simulation was repeated for a hypothetical carbonaceous chondrite meteoroid ($\sigma = 0.042 \text{ s}^2 \text{ km}^{-2}$,
 171 $\rho_m = 2000 \text{ kg m}^{-3}$, τ for Type II bodies [43, 60]) with the same 20 kg mass, and the meteoroid only
 172 penetrated down to 53 km while the simulated light curve was ~ 2.5 magnitudes brighter than observed.
 173 We found no combination of model parameters for cometary or carbonaceous-chondrite-like material which
 174 could fit the observations.

175 As shown in Figure 3, the meteoroid fragmented in a similar way as ordinary chondrites, with the earliest
 176 significant fragmentation occurring around 100 kPa, and the final one around 1 MPa [36]. However, the body
 177 never catastrophically disrupted into constituent grains, even after reaching a maximum dynamic pressure
 178 of 2 MPa, a further indication that it was very strong. There were also minor episodes of fragmentation
 179 around 400 kPa.

180 It is possible to estimate the flux and the ratio of Type I (rocky) objects in comparison to weaker Type
 181 II/III from the Oort cloud at the limiting mass appropriate for fast fireballs. The only published data sets for
 182 which there are reliable mass and time-area product estimates are the Meteorite Observation and Recovery
 183 Project (MORP)[61], European Network (EN)[62, 63], and Prairie Network (PN)[35] data sets. There are

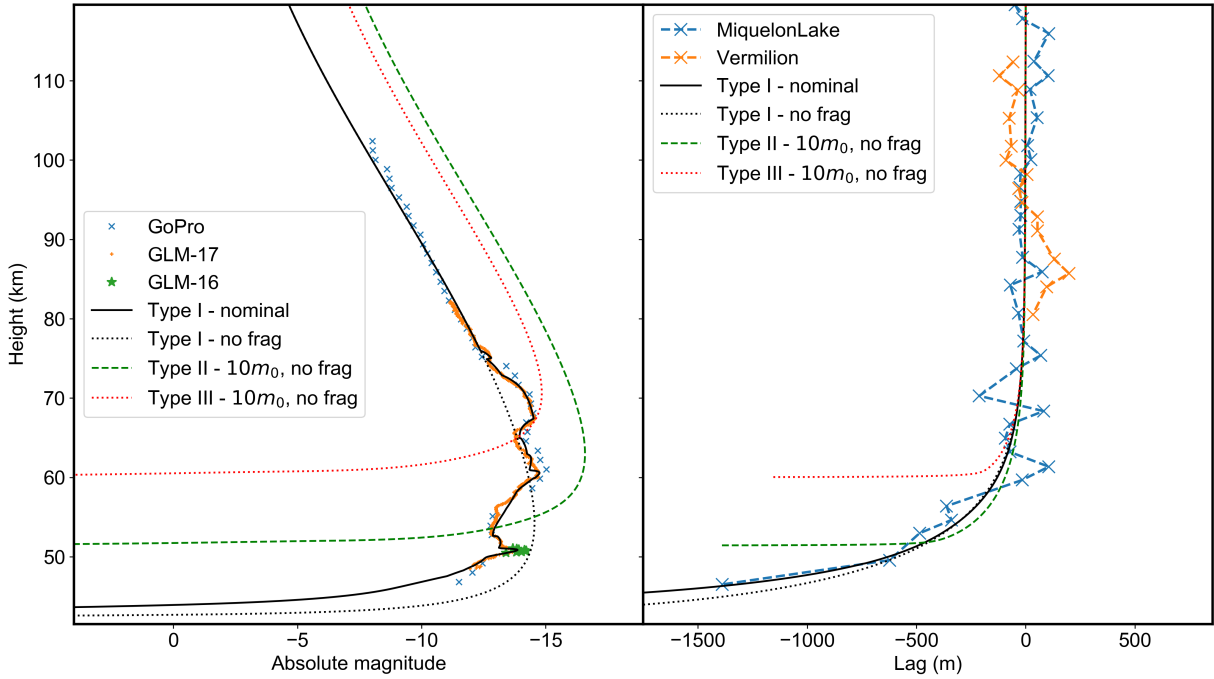


Figure 2: Left: Observed and simulated light curve. The solid black line is the nominal fit with the parameters and fragmentation behaviour given in Tables 9 and 8. A no-fragmentation solution for Type I (black), II (green), and III (red) objects is also shown. Note that the GLM lightcurve was calibrated using three independent high speed fireballs where GLM lightcurves and ground-based records were available (see Methods for details). Right: Observed and simulated deceleration profile (lag) for various simulation scenarios. The lag is the distance a decelerating meteoroid falls behind a hypothetical non-decelerating meteoroid moving at the initially observed velocity. The Cochran security camera was not used for velocity measurement due to lower accuracy.

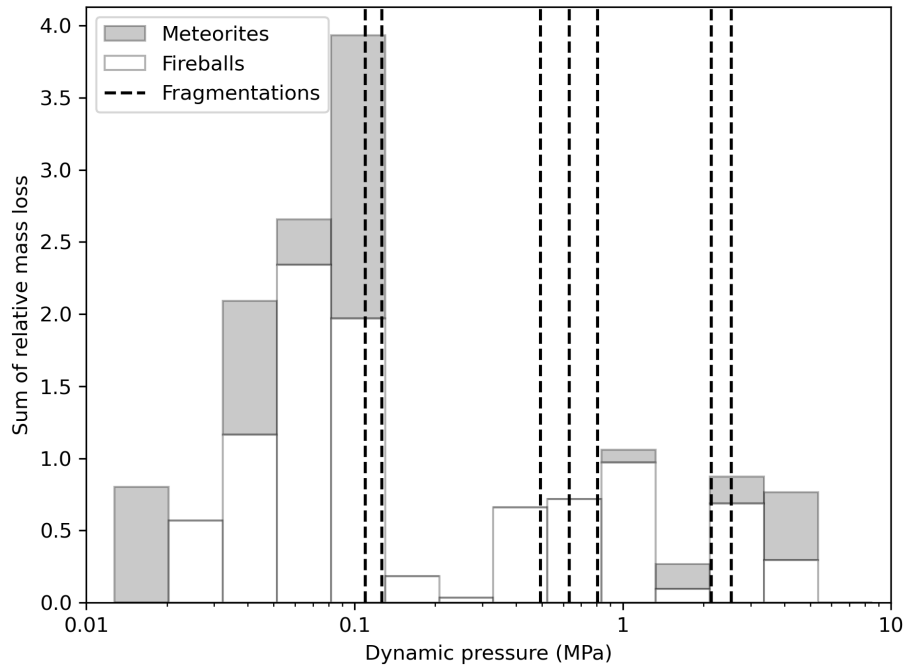


Figure 3: Observed fragmentations of the Alberta meteoroid (vertical dashed lines) overlaid on top of previously observed fragmentation behaviour of meteorite-dropping fireballs. The dynamic pressure was normalized to $\Gamma = 1.0$ to be consistent with values from ref. [36]. The gray bars show the sum of relative mass loss at the given dynamic pressure for fireballs with recovered meteorites, and white bars are for ordinary chondrite fireballs with currently unrecovered meteorites (data from ref. [36]).

Table 3: Table of all $T_J < 2$ Type I objects found in literature satisfying our criteria. The mass is given in the ref. [35] scale. Note that the modern photometric mass scale is an order of magnitude smaller [36].

Name	PE	T_J	Mass (kg)	a (au)	q (au)	e	i (deg)	ω (deg)	Ω (deg)
Alberta (this work)	-4.49	-0.46	13.3	104	0.615	0.994	121.40	104.0	333.86
Karlštejn[56]	-4.53	0.64	1.5	3.5	1.012	0.710	137.90	174.6	71.55
MORP #434[61]	-4.54	0.77	0.005	5.5	0.236	0.957	107.6	303.7	256.4
MORP #441[61]	-4.04	-0.78	0.020	24.7	0.765	0.969	159.7	56.7	103.8

184 a total of 41 fireballs with $T_J < 2$ and speed $> 50 \text{ km s}^{-1}$ in those data sets. The speed limit removes the
185 speed-dependent mass sensitivity [43], so we can set a hard limiting mass for the flux. We set the mass limit
186 to 10 g (ref. [35] mass scale), for which these data sets are complete, leaving a total of 32 fireballs. This
187 mass is also significantly larger than any previously observed refractory inclusions in cometary material; the
188 largest Type I Taurids are an order of magnitude smaller [1].

189 Of those 32, two are Type I objects (MORP catalog #434 with $m = 5 \text{ g}$ and #441 with $m = 20 \text{ g}$) which
190 were also on retrograde orbits ($e = 0.957$, $i = 107.6^\circ$, and $e = 0.969$, $i = 159.7^\circ$). All Type I objects used
191 for our flux estimate are an isolated group, have $T_J < 1$, retrograde orbits, and are quite far from the PE
192 dividing line for Type II objects (see Figure 4 and Table 3). As these objects have a mass similar to the
193 largest refractory inclusions in Taurids, they cannot be excluded as constituents of comets though they are
194 observed on very different orbits from the Taurids. We only use these additional meteoroids to set an upper
195 bound on the flux of Type I objects from the Oort cloud.

196 The total time-area product for the PN survey is $10^{11} \text{ km}^2 \text{ h}$, and for MORP is $1.5 \times 10^{10} \text{ km}^2 \text{ h}$ [64].
197 The EN data set used here is only complete up to 1996, at which time the time-area product of the survey
198 was $2 \times 10^{11} \text{ km}^2 \text{ h}$. The network did not observe any other fireball similar to the Karlštejn event up until
199 the present date (mid-2021) at which time the time-area product increased to $4 \times 10^{11} \text{ km}^2 \text{ h}$ (Pavel Spurný,
200 private communication). The time-area product of the fireball network in Alberta (MORP2.0) which observed
201 the featured event is not taken into account. The network was deployed only very recently (late 2019) with
202 a small number of stations. We estimate its time-area product to be on the order of $10^9 \text{ km}^2 \text{ h}$, less than
203 1% of the sum time-area product of the other networks.

204 Thus the total time-area product for $T_J < 2$ Type I events is $5.15 \times 10^{11} \text{ km}^2 \text{ h}$, and for all $T_J < 2$ Type II
205 and III objects in our data is $3.15 \times 10^{11} \text{ km}^2 \text{ h}$. From this we compute a total flux of Type I object on LPC-
206 type orbits as 0.34-0.67 meteors/ $10^6 \text{ km}^2/\text{yr}$ (the upper bound depending on if the smaller MORP objects
207 are included), while the flux of Type II and III objects on LPC-type orbits is 11.25 meteors/ $10^6 \text{ km}^2/\text{yr}$
208 to the limiting mass of 0.01 kg. We estimate from these data that the relative abundance of macroscopic
209 ($>0.01 \text{ kg}$) Type I objects on $T_J < 2$ orbits is therefore between 3% and 6% of all meteoroids impacting
210 Earth on LPC-like orbits.

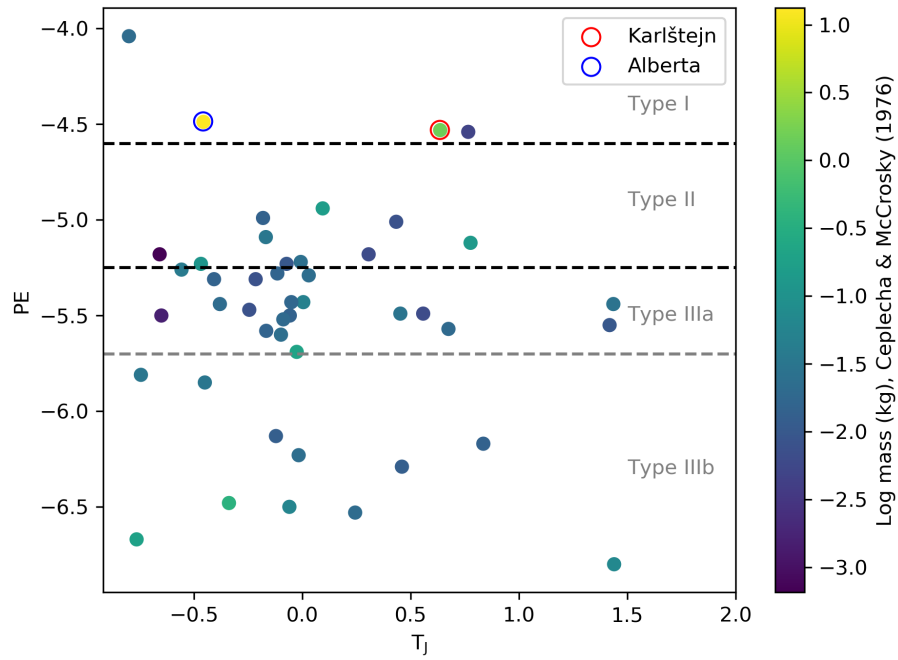


Figure 4: All published fireball data showing PE as a function of Tisserand’s parameter with respect to Jupiter for $T_J < 2$ fireballs in the MORP, EN, and PN data sets. The Type I objects of interest above the $PE = -4.6$ dividing line between Type I/II fireballs form a clearly separate grouping. Note that the Alberta fireball is the largest mass fireball of any type recorded on an LPC orbit to date.

211 Discussion

212 The confirmation of the existence and a comparatively high abundance of macroscopic lithic objects in
213 the Oort cloud supports the need for a mechanism of ejection of inner Solar System material into nearly
214 hyperbolic orbits. Even in a scenario where most of the Oort cloud objects are captured from other star
215 systems [65], an ejection mechanism still needs to be present to explain the radial mixing of material. Our
216 findings support a massive proto-asteroid belt scenario as the source of these objects, although the exact
217 mechanism of its depletion still remains elusive. The dynamical instability caused by Jupiter remains the
218 most plausible candidate. These findings challenge Solar System formation models based on pebble accretion
219 alone.

220 Our estimated range in abundance of rocky objects with masses larger than 0.01 kg of 3% to 6% is higher
221 than model-predicted values. This may indicate either an order of magnitude more massive proto-asteroid
222 belt than traditionally assumed, a higher Oort cloud capture efficiency of scattered inner Solar System
223 material, or a mass distribution in the proto-asteroid belt heavily favouring smaller objects.

Table 4: Geographical coordinates of the optical cameras used in this work.

Name	Field of view	Latitude (+N)	Longitude (+E)	Elevation (mean sea level)
GFO Miquelon Lake	all-sky	53.239340°	-112.889855°	785 m
GFO Vermilion	all-sky	53.338975°	-110.884085°	624 m
Cochrane	134° × 105°	51.224138°	-114.706921°	1213 m
GoPro (photometry)	140° × 90°	50.910076°	-114.038749°	1040 m

Methods

0.1 Astrometric calibration

The most critical measurement leading to the core result in this work (the unusually low end height for such a high velocity fireball) is directly derived from the optical observations of the event. Thus, the quality of the astrometric calibration and measurements are of paramount importance. In this section we present the calibration details for each of the three optical instruments used to derive the trajectory. These include two Global Fireball Observatory (GFO) high resolution dedicated fireball cameras (one at Miquelon Lake the other near Vermilion, Alberta) and one security camera (located in Cochrane, Alberta outside of Calgary). The camera locations are given in Table 4 and shown in relation to the fireball in Figure 5.

0.1.1 Global Fireball Observatory data

The GFO all-sky cameras operated by the MORP2.0 project produce 7340×4930 px color images with an exposure time of 27 s and 16 bits of depth. Electronic liquid crystal shutters are toggled to encode the timing information into the image. The shutters produce 20 segments per second, and the segments are encoded as a Debruijn sequence of ones and zeros [66] so that the absolute time of every segment can be derived. In combination with the Samyang 8 mm f/3.5 fish-eye lens, the images have a plate scale of 2 arcmin px^{-1} .

The astrometric fit was performed with a radial distortion model [5] using odd polynomial coefficients up to the 7th order, asymmetry correction, and a fixed aspect ratio. Including the pointing direction (reference right ascension, declination, position angle, and the plate scale), the fit uses a total of 11 free parameters.

Figure 6 shows the fit residuals for the Miquelon Lake camera. The mean angular forward mapping (image to sky) error was 0.49 arcmin, with a fit showing no trends in residuals with radius from the centre of the image but a slight systematic trend in the azimuth. We believe that the main cause of the trend is a higher order component of asymmetry in the optics not captured by the distortion model, as the point-spread function was significantly variable across the field of view. Nevertheless, this offset is only on the order of 0.5 arcmin, i.e. 20 m at the range of the fireball from the station and does not significantly influence the final result. The fireball covered azimuths from 30° to 350° (counter-clockwise) and elevations from 54° to 15.7°, ranges well covered by available calibration stars.

The astrometric fit for the Vermilion GFO station was not as good, having root mean square fit residuals

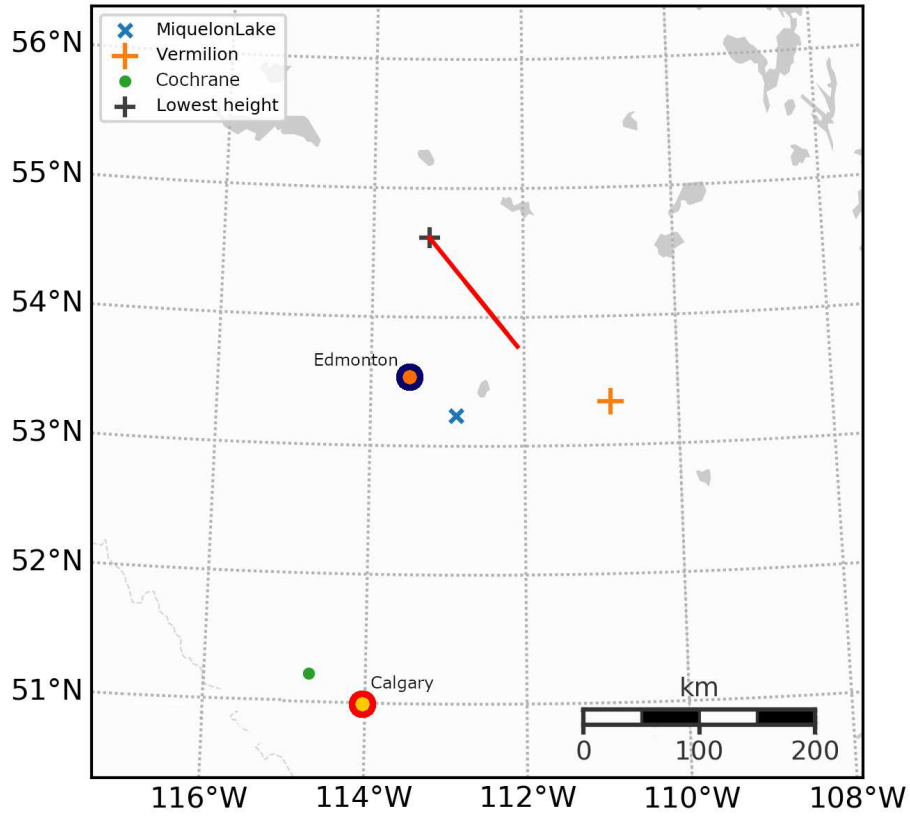


Figure 5: Map showing the location of the fireball trajectory (red line), cameras, and major population centers in Calgary and Edmonton. The GoPro camera was located in Calgary.

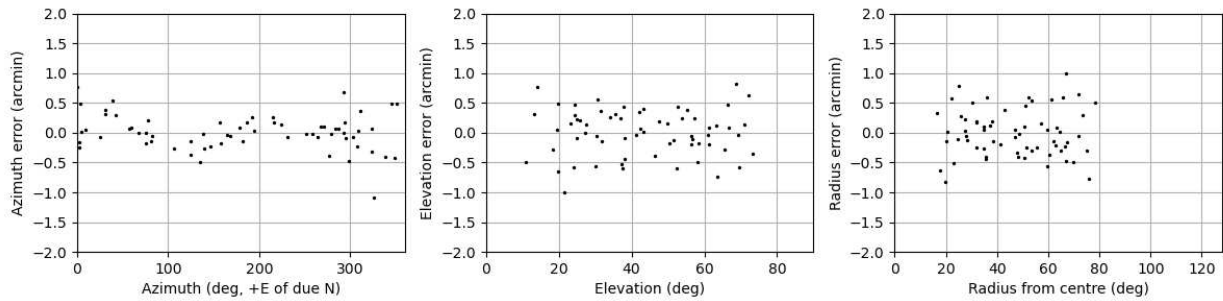


Figure 6: Astrometric calibration fit using a 7th order polynomial (odd-terms only) radial distortion model for the Miquelon Lake camera. Forward mapping (image to sky) errors.

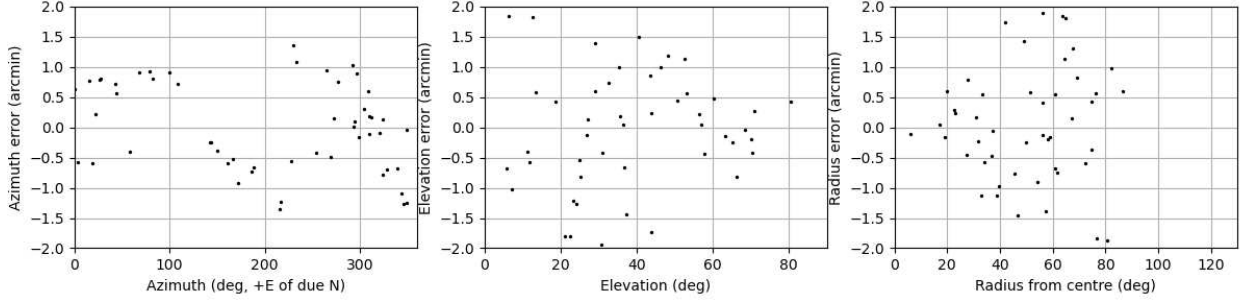


Figure 7: Astrometric calibration fit for the Vermillion camera. Forward mapping (image to sky) errors.

251 of 1.37 arcmin, as shown in Figure 7. This decrease in accuracy was caused by a more non-Gaussian point-
 252 spread function than for the Miquelon Lake camera. However, the absolute accuracy remained high – the
 253 corresponding linear error was only 65 m at the range of the fireball. The fireball had a nearly constant
 254 azimuth of 310° and covered elevations from 43° to 11° , ranges for which there were many stars in the
 255 calibration.

256 0.2 Security camera calibration

257 Despite the good geometry and high accuracy of GFO measurements (convergence angle of 46.5° and spatial
 258 trajectory fit residuals of ~ 30 m), a two-station trajectory solution can suffer from systematic biases due
 259 to meteor-station geometry [67, 68]. As a further constraint, we included additional measurements from a
 260 Google Nest doorbell camera in Cochrane, Alberta, 50 km west of Calgary.

261 The radial distortion model with odd terms up to the fifth order was used for calibration [5]. The model
 262 has a total of eight parameters and eight stars were used in the fit (Figure 8). The average fit error was
 263 4 arcmin. Only the first half of the fireball was used in the trajectory solution as the camera saturated
 264 and skipped frames during the brightest phase. The difference in the geocentric radiant with and without
 265 the security camera measurements was only 0.03° , and 0.14 km s^{-1} in geocentric speed, indicating that the
 266 GFO-only solution had no major systematic errors.

267 0.3 Trajectory details

268 Figure 9 shows the trajectory fit residuals and the observed deceleration. The trajectory fit is tight and
 269 within the expected astrometric accuracy. The fireball did not show much deceleration before a height of
 270 60 km. The initial velocity was computed as the average velocity above the height of 70 km.

271 The reference time for the trajectory is 2021-02-22 13:23:17.683 UTC (Julian date 2459268.057843548711).
 272 The state vector in the Earth-centered inertial (ECI) coordinates in the epoch of date are given in Table



Figure 8: Composite of frames from the Cochrane security camera video showing the fireball and the calibration stars (marked with a white letter C), four of which were in Cassiopeia. An equatorial grid is laid over the video with catalog stars shown as red crosshairs.

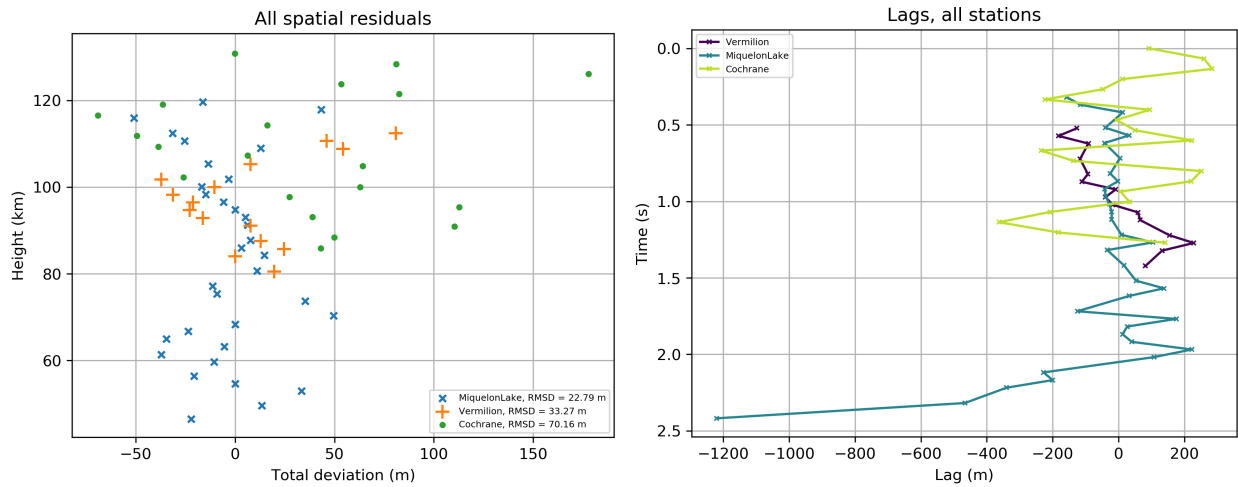


Figure 9: Left: Spatial trajectory fit residuals versus height. Right: The observed lag (“the distance that the meteoroid falls behind an object with a constant velocity that is equal to the initial meteoroid velocity” [69].)

Table 5: ECI trajectory state vector.

$X =$	-1844963	\pm	44	m
$Y =$	-3384728	\pm	193	m
$Z =$	5227379	\pm	153	m
$V_X =$	2161	\pm	41	m/s
$V_Y =$	-61705	\pm	15	m/s
$V_Z =$	5244	\pm	155	m/s

Table 6: ECI state vector covariance matrix.

	X (m)	Y (m)	Z (m)	V_X (m/s)	V_Y (m/s)	V_Z (m/s)
X	+1.778e+03	+4.430e+02	+4.577e+03	+1.499e+03	+8.165e+02	+4.720e+03
Y	+4.430e+02	+3.851e+04	-7.591e+02	+1.377e+03	+4.232e+03	+2.417e+03
Z	+4.577e+03	-7.591e+02	+2.168e+04	+4.334e+03	+2.671e+03	+2.039e+04
V_X	+1.499e+03	+1.377e+03	+4.334e+03	+1.491e+03	+9.583e+02	+4.765e+03
V_Y	+8.165e+02	+4.232e+03	+2.671e+03	+9.583e+02	+1.448e+03	+3.880e+03
V_Z	+4.720e+03	+2.417e+03	+2.039e+04	+4.765e+03	+3.880e+03	+2.163e+04

273 5, and the state vector covariance matrix is given in Table 6, and the orbital covariance matrix is given in
 274 Table 7.

275 0.4 Orbital integration

276 To investigate the influence of planetary interactions with the meteoroid’s orbit, we backtracked 100 clones
 277 within the measured uncertainty. Because of its high inclination, the only appreciable approaches to the
 278 planets are at its other (ascending) node, which is near Mars’ orbit. However, no clone passed closer than
 279 1.1 AU from this planet. Figure 10 shows the variation in the heliocentric elements as a function of distance
 280 from Mars. The simulations start 60 days prior to impact and run for 365 days further back. A slight jump
 281 in each of the elements can be seen at the minimum distance from Mars, but it is small: it will not affect a
 282 potential parent body search and does not affect the proposed origin of the object.

283 Note that the orbital elements do not become completely constant even well after the Mars encounter.
 284 This is because they are heliocentric elements, and for such a large semi-major axis orbit, Jupiter’s tug both
 285 on the Sun and the object create ongoing small changes. Even if the orbital elements were considered in the
 286 barycentric frame, the effect of ongoing planetary perturbations on such loosely bound orbits means that

Table 7: Orbital covariance matrix. T_p is the Julian date of last perihelion (nominal $T_p = 2459230.729594$).

	e	q (au)	T_p (day)	Ω (deg)	ω (deg)	i (deg)
e	+8.321e-06	+4.075e-06	+2.410e-04	+1.762e-08	+6.764e-04	-5.763e-04
q	+4.075e-06	+2.367e-06	+1.240e-04	+1.009e-08	+3.757e-04	-3.302e-04
T_p	+2.410e-04	+1.240e-04	+7.079e-03	+5.341e-07	+2.031e-02	-1.746e-02
Ω	+1.762e-08	+1.009e-08	+5.341e-07	+5.399e-11	+1.607e-06	-1.767e-06
ω	+6.764e-04	+3.757e-04	+2.031e-02	+1.607e-06	+6.030e-02	-5.258e-02
i	-5.763e-04	-3.302e-04	-1.746e-02	-1.767e-06	-5.258e-02	+5.786e-02

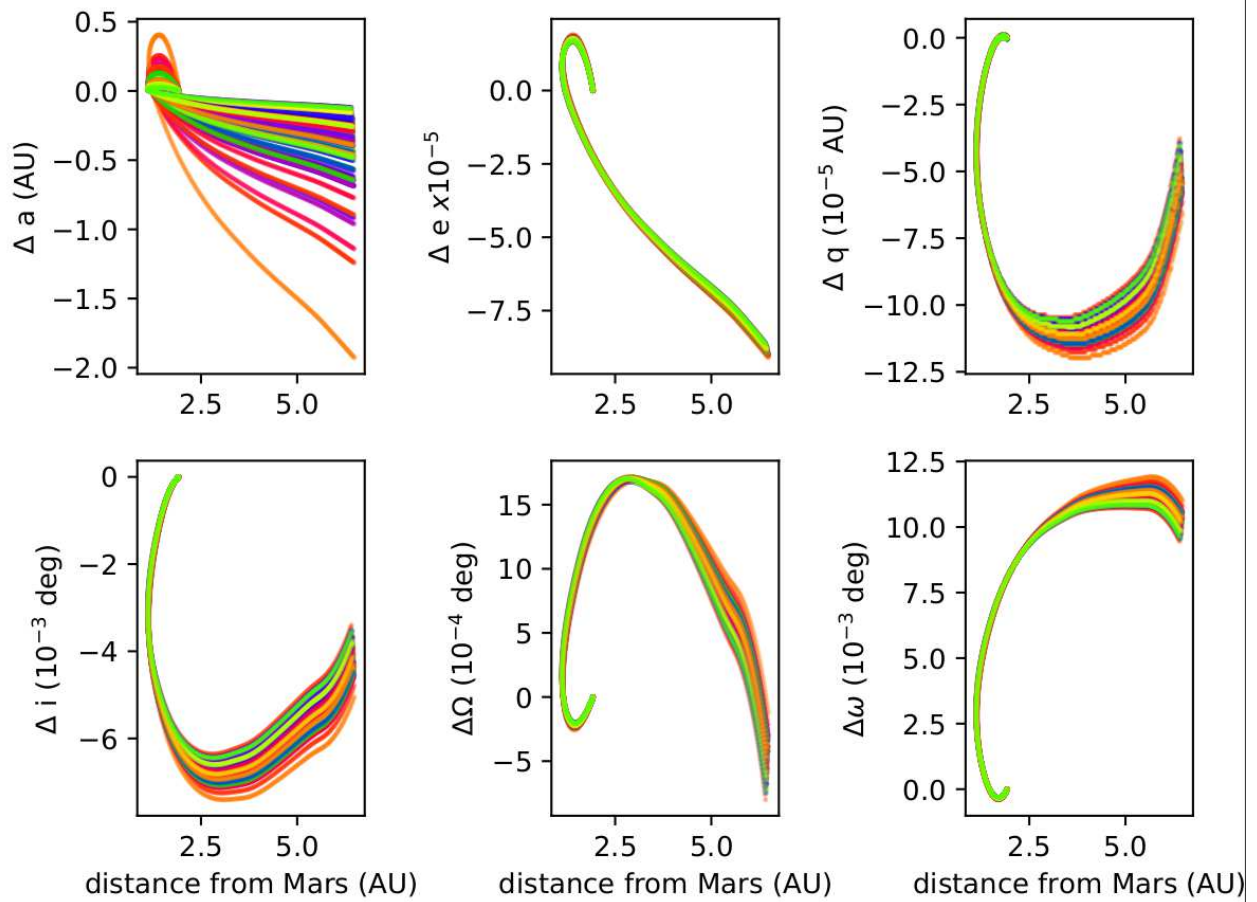


Figure 10: Change in orbital elements over time, between -60 and -365 days before impact. Time is not shown on any axis, but the clones that start at $t - 60$ days are clustered at zero and spread out as we go further back in time, as the distance from Mars decreases and then increases again.

287 the orbital elements will have trends over time regardless of the reference frame.

288 0.5 Photometric calibration

289 To fully model the fragmentation behaviour of a meteoroid, it is necessary to have a well-calibrated light
290 curve. The Alberta event was observed by both space-based GLM instruments and one fixed GoPro HERO5
291 action camera in Calgary (~ 400 km from the fireball). The resulting calibrated light curves are given in
292 Figure 2. Note that the GFO cameras used for astrometry were partially saturated over the height range
293 of interest and therefore not used in the photometric calibration. However, as the Nikon D810 used by the
294 GFO have CMOS (and not CCD) chips for imaging, even in saturation the astrometry is reliable [5].

295 The GoPro camera had a low sensitivity and in conjunction with the large range to the fireball it was able
296 to capture the whole fireball without saturating despite only having 8 bits of depth. As the camera did not
297 observe any stars, the absolute calibration was done indirectly using seven distant streetlights visible in the
298 video. A separate DSLR photo of stars and the streetlights was taken – the magnitudes of the streetlights
299 were measured on the DSLR photo and used as a basis for the GoPro calibration. The mean photometric
300 error was 0.27 magnitudes and the vignetting coefficient was estimated to be $0.001 \text{ rad px}^{-1}$ (see ref. [5]).

301 An attempt was made to measure the photometry from scattered light on the Cochrane security camera
302 video (method of ref. [70]), but the camera had a wide dynamic range (WDR) feature. This produces image
303 levels that are not linear responses to light and was thus not able to be used. Such image enhancement
304 features may prevent using modern security cameras for scattered light fireball photometry in the future.

305 Converting the energy observed by the GLM into magnitudes is challenging due to its narrow 1.1 nm
306 pass band around 777.4 nm, making it necessary to assume a spectral energy distribution to compute a
307 bolometric magnitude. For slower meteoroids such as meteorite-dropping fireballs, it is possible to assume a
308 blackbody spectrum and derive a conversion [7], but at high speeds elemental and atmospheric lines are more
309 pronounced making the blackbody assumption invalid. Furthermore, the intensity of the oxygen triplet line
310 that the GLM is observing was found to significantly increase with meteoroid speed [71]. For these reasons,
311 we performed a manual calibration between the GLM group energy and magnitude using three fast and bright
312 (around -11^M) fireballs observed by NASA MEO all-sky cameras [72] and AMOS systems [2]. Among many
313 fireballs observed by these systems, only two fireballs observed with NASA systems had GLM light curves
314 and were observed sufficiently far away not to saturate the cameras. Some saturated frames in the AMOS
315 recording (2020/10/19 12:42:55 UTC) were corrected using a calibration curve for saturated pixels, based
316 on calibrated measurements of bright planets and Moon in different phases. The in-atmosphere speeds of
317 the fireballs were 58, 66, and 69 km s^{-1} . We used the classical equation to compute the magnitude:

$$M = -2.5 \log E_G + p_0 \tag{1}$$

318 where E_G is the GLM group energy in femtojoules and the p_0 is the photometric offset in magnitudes. For
 319 all three fireballs, the GLM light curves matched best for $p_0 = -9.2$, with an error of ± 0.1 mag. The
 320 comparison between the optical and GLM light curves is shown in Figure 11.

321 0.6 Ablation and fragmentation model

322 The dynamics and light curve of the fireball were simulated using an established semi-empirical model [41]
 323 which was successfully applied to reconstruct the fragmentation behaviour and physical properties of many
 324 meteorite dropping fireballs [73, 74, 75, 36] and fainter meteors [38, 39]. In this model, the meteoroid
 325 is initially treated as a single body, but increases in brightness and sudden deceleration are explained by
 326 fragmentation. Previous works established several main modes of fragmentation: splitting into several single-
 327 body fragments, steady erosion of $10 \mu\text{m} - 1 \text{ mm}$ sized refractory constituent grains from the meteoroid's
 328 surface, ejection of an eroding fragment, and a sudden release of dust (i.e. a large number of constituent
 329 grains)[41].

330 All fragments and grains are modelled using the classical equations of single-body ablation [43]:

$$\frac{dv}{dt} = -Km^{-1/3}\rho_{\text{air}}v^2, \quad (2)$$

$$\frac{dm_a}{dt} = -K\sigma m^{2/3}\rho_{\text{air}}v^3, \quad (3)$$

331 where K is the shape density coefficient, m the meteoroid mass (m_a is the ablated mass), v the velocity, ρ_{air}
 332 the atmosphere bulk density (NRLMSISE-00 model [76]), and σ is the ablation coefficient. The parameter
 333 K is used because the meteoroid density and shape cannot be measured separately:

$$K = \Gamma A \rho_m^{-2/3}, \quad (4)$$

334 where Γ is the drag coefficient, A is the shape coefficient (1.21 for spheres which we adopt), and ρ_m is the
 335 meteoroid (or grain) bulk density. The equations were numerically integrated using a 4th order Runge-Kutta
 336 method and a time step of 2 ms. The integration of individual fragments is stopped if their mass falls below
 337 10^{-14} kg or the speed below 3 km s^{-1} , which is the ablation limit [43].

338 The luminosity produced by ablation is computed as:

$$I = -\tau \frac{v^2}{2} \frac{dm_a}{dt}, \quad (5)$$

339 where τ is the luminous efficiency. We ignore the deceleration term as it is not significant at high speeds
 340 [43]. In this work we use the modern luminous efficiency function of ref. [36] to model the observed event.

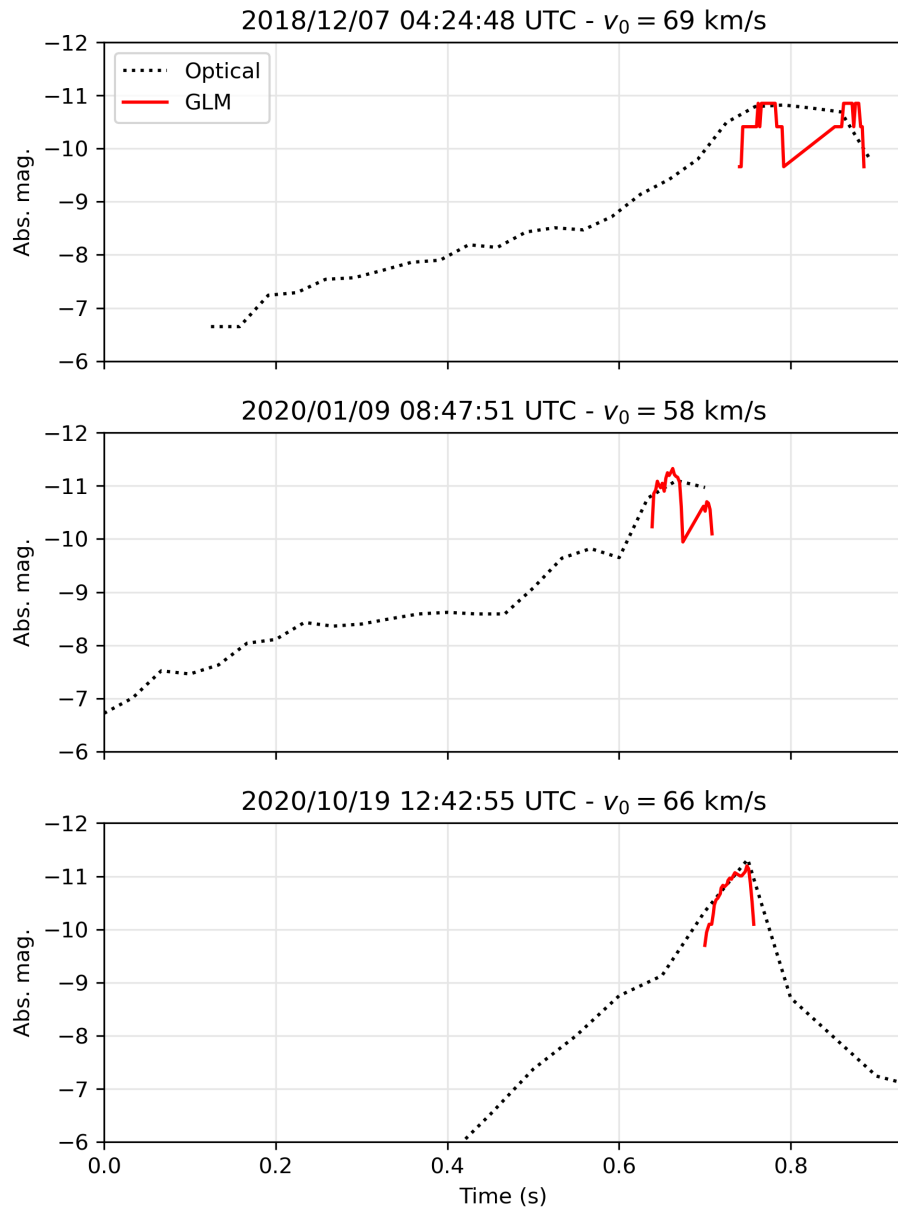


Figure 11: Comparison between optical light curves and GLM-derived light curves of calibration fireballs using Equation 1.

341 If the meteoroid or an ejected fragment is set to erode at a given time in the model, the total mass
 342 lost in erosion is regulated by the erosion coefficient η which is applied in the same manner as the ablation
 343 coefficient in equation 3:

$$\frac{dm_e}{dt} = -K\eta m^{2/3} \rho_{\text{air}} v^3. \quad (6)$$

344 For grain bulk density, we use 3500 kg m^{-3} , appropriate for refractory silicate grains. The total mass loss
 345 at a given time is then the sum of the ablation and erosion mass loss:

$$\frac{dm}{dt} = \frac{dm_a}{dt} + \frac{dm_e}{dt}. \quad (7)$$

346 Inspired by in-situ observations of the mass distribution of cometary dust [40], the masses of eroded
 347 grains are distributed according to a power-law $n(m) \sim m^{-s}$ (ref. [77]) where $n(m)$ is the number of grains
 348 of a given mass m , and s is the differential mass distribution index. An upper (m_u) and a lower (m_l) grain
 349 mass limit is set during modelling to reproduce higher frequency components of the lightcurve. To speed up
 350 computation, the mass range is binned into z bins per order of magnitude, thus the integration of ablation
 351 equations is done only once for every mass bin instead for every fragment. A mass sorting parameter can
 352 be defined as $p = 10^{1/z}$ and it follows that the total number of grain mass bins within a range of masses is
 353 $k = \lceil \log(m_l/m_u) / \log p \rceil$. The total number of grains having a mass equal to the upper mass limit is then:

$$n_u = \begin{cases} \frac{m_e}{km_u}, & \text{for } s = 2 \\ \frac{m_e}{m_u} \frac{1-p^{(2-s)}}{1-p^{k(2-s)}}, & \text{for } s \neq 2, \end{cases} \quad (8)$$

354 where m_e is the total eroded mass at the given time step. The mass of every bin i is then $m_i = m_u p^i$ for
 355 $i = 0, 1, \dots, k-1$. The number of discrete grains N_i in every bin can be computed as:

$$n_i = n_u (m_u/m_i)^{(s-1)} + \frac{\Delta m_{i-1}}{m_i}, \quad (9)$$

$$N_i = \lfloor n_i \rfloor, \quad (10)$$

356 where $\Delta m_i = m_i(n_i - N_i)$ is the leftover mass in the mass bin after making the number of grains discrete
 357 ($\Delta m_0 = 0$). The leftover masses from the larger mass bins is distributed into smaller mass bins to ensure
 358 that there is no "virtual" mass loss due to numerical rounding. The grains are then ablated as single bodies
 359 until exhaustion following equations 2 and 3. A separate luminosity I_i is computed for every mass bin, and
 360 the total luminosity produced by all grains at a given time is simply $\sum_{i=0}^{k-1} N_i I_i$.

361 Finally, after all fragments and grains have been fully integrated and their masses depleted, the magnitude

Table 8: Fragmentation behaviour. The total mass of all ejected fragments is 1.04 kg. The fragment mass percentage in the table is reference to the mass of the main fragment at the moment. The mass distribution index for all grains was $s = 2.0$. The values of the dynamic pressure are computed using the drag coefficient Γ used in the modelling for the appropriate height, as described in Table 9.

Time ^a (s)	Height (km)	Velocity (km s ⁻¹)	Dyn pres (MPa)	Main m (kg)	Fragment	m (%)	m (kg)	Erosion coeff (s ² km ⁻²)	Grain m range (kg)
1.49	76.0	62.03	0.09	1.73	EF	8	0.139	0.030	10 ⁻⁷ - 10 ⁻⁶
1.52	75.0	62.02	0.10	1.59	EF	20	0.317	0.035	10 ⁻⁶ - 10 ⁻⁴
1.57	73.0	62.00	0.10	1.25	EM	-	-	0.030	10 ⁻⁶ - 10 ⁻⁵
1.72	67.5	61.88	0.21	0.93	EM	-	-	OFF	-
1.79	65.0	61.78	0.30	0.87	EF	35	0.310	0.020	10 ⁻⁵ - 10 ⁻³
1.84	63.0	61.66	0.38	0.54	EF	15	0.081	0.020	10 ⁻⁷ - 10 ⁻⁶
1.90	61.0	61.49	0.48	0.42	EF	18	0.075	0.080	10 ⁻⁷ - 10 ⁻⁶
2.12	52.7	59.84	1.28	0.17	EF	50	0.084	0.005	10 ⁻⁴ - 10 ⁻³
2.17	51.2	59.07	1.52	0.06	EF	50	0.030	0.050	10 ⁻⁶ - 10 ⁻⁵

^a Seconds after 13:23:17.683 UTC.

EM = Main fragment erosion; EF = New eroding fragment.

362 M of the fireball as it would be seen at a distance of 100 km is computed as:

$$M = -2.5 \log \frac{I}{P_{0m}}, \quad (11)$$

363 where P_{0m} is the power that a meteor needs to radiate in the camera's spectral band-pass so that it has an
364 apparent magnitude of 0^M at a range of 100 km. In this work, we use a value of 1300 W, as appropriate for
365 a high-speed meteor in the spectral band-pass of CMOS/CCD sensors [78].

366 0.7 Modelling results

367 We model the fragmentation behaviour of the fireball in two ways. (1) by direct erosion of the main body
368 (EM), and (2) by ejecting larger fragments which erode independently (EF). Figure 12 shows the details of
369 the fragmentation on the simulated light curve which are also listed in Table 8, and Figure 13 shows the
370 mass loss with increasing dynamic pressure. The modelled physical properties of the fireball are given in
371 Table 9.

372 Because this fireball is much different from other modelled fireballs (large, high speed rocky meteoroid
373 reaching low altitude), there were several differences and uncertainties in chosen parameters as compared to
374 low-velocity Type I objects:

- 375 1. The luminous efficiency for Type I objects at high speeds is unknown, as this is the first object of this
376 kind to be observed. We used the model of ref. [36] which suggest a value of $\sim 14\%$ for 1 kg objects
377 and $\sim 10\%$ for grains. If the luminous efficiency is akin to low-speed meteorite dropping fireballs
378 ($\sim 5\%$), the initial mass is $\sim 3\times$ larger (6 kg), but the identification of the meteoroid as a Type I

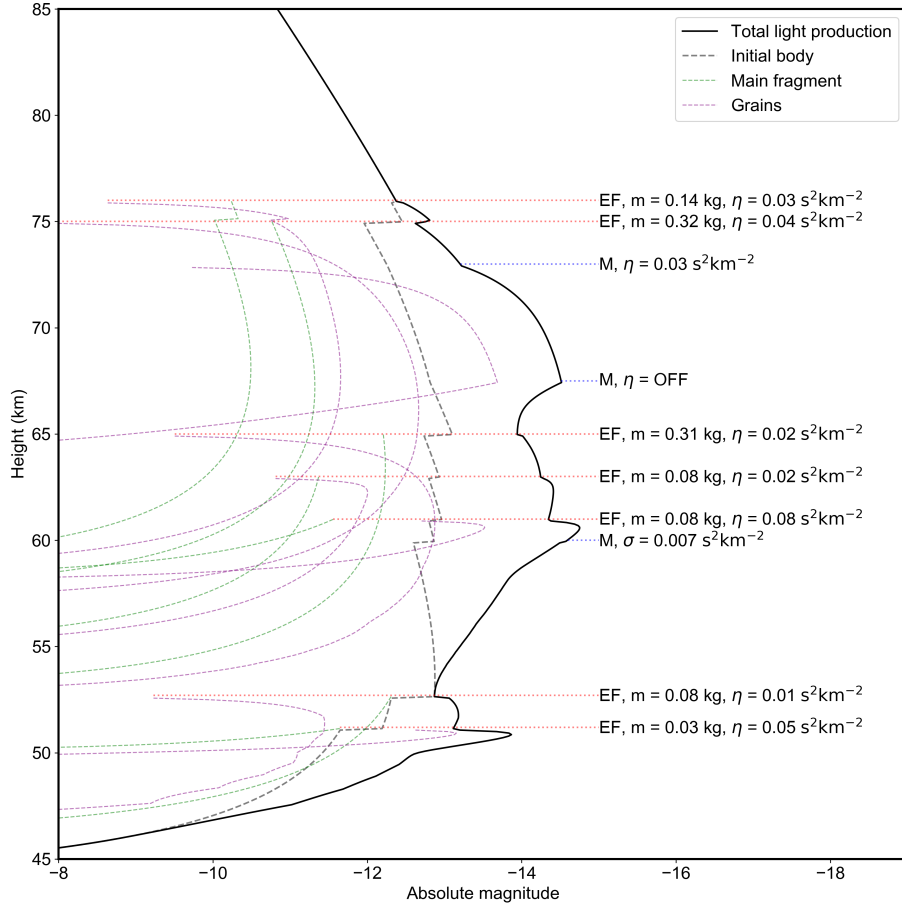


Figure 12: Details of the modelled individual fragmentations of the meteoroid marked on the simulated light curve. Solid black line is the total light production, the dashed black line is the magnitude of the main body from which fragments are released, green dashed lines are magnitudes of the eroding fragments, and purple lines are magnitudes of the grains ejected either from the main body or the eroding fragments.

Table 9: Modelled physical properties. The mass was computed using a modern luminous efficiency model of [54] which results in an order of magnitude smaller mass estimates than the ref. [35] model used for PE computation.

Description		Value
Initial mass (kg)	m_0	1.8
Initial speed at 180 km (km s^{-1})	v_0	62.10
Zenith angle	Z_c	54.885°
Bulk density (kg m^{-3})	ρ	3300
Grain density (kg m^{-3})	ρ	3500
Ablation coefficient ($\text{s}^2 \text{ km}^{-2}$)	σ	0.009
(below 60 km)	σ	0.007
Shape factor (sphere)	A	1.21
Drag coefficient	Γ	0.8
(below 75 km)	Γ	0.6

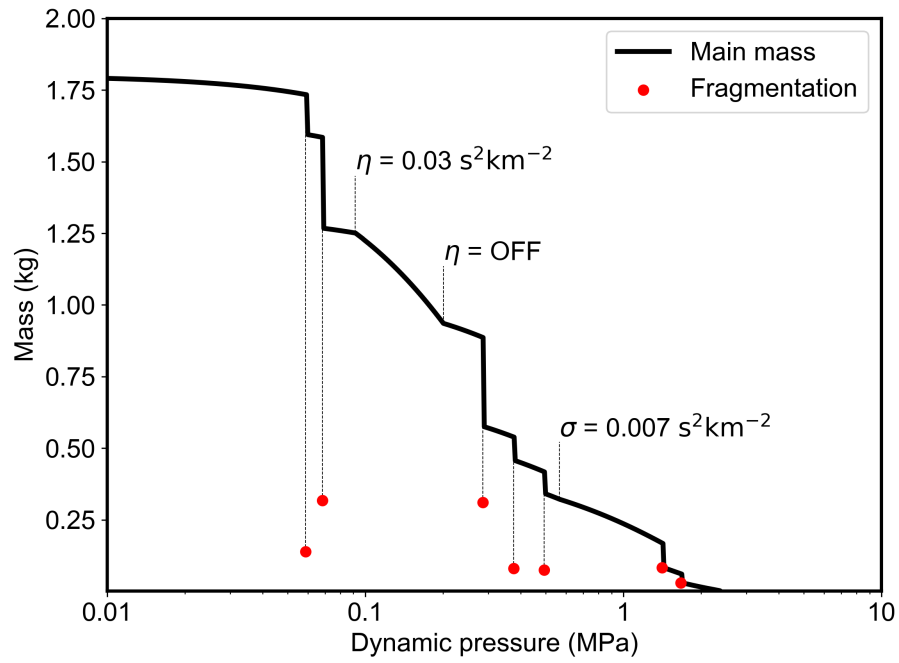


Figure 13: Modelled mass loss as a function of increasing dynamic pressure. Model fragmentation points and masses of major fragments are marked with red circles. η marks the change in the erosion coefficient, and σ the change in the ablation coefficient of the main body.

379 fireball is unchanged.

380
381 2. A higher intrinsic ablation coefficient of $0.009 \text{ s}^2 \text{ km}^{-2}$ (and $0.007 \text{ s}^2 \text{ km}^{-2}$ below 60 km) was used,
382 compared to $0.005 \text{ s}^2 \text{ km}^{-2}$ for low-velocity deeply penetrating fireballs [43].

383
384 3. The model matches the light curve well even at the beginning of luminous flight at fainter magnitudes.
385 This is not usually the case for slower meteorite-dropping fireballs as they undergo a period of pre-
386 heating, and the classical equations do not capture that complexity in those cases.

387 388 0.8 Computing PE

389 The PE criterion was derived as an empirical tool to help easily differentiate between different material
390 types [35] without the complexity of full numerical ablation modelling. It was based on well understood
391 relationships between physical properties of meteoroids and their observed behaviour as they enter the
392 atmosphere.

393 It is defined as:

$$PE = \log \rho_E - 0.42 \log m_0 + 1.49 \log v_0 - 1.29 \log \cos Z_C \quad (12)$$

394 where ρ_E is the atmosphere mass density at the end height of the fireball in g cm^{-3} , m_0 is the initial mass
395 in grams, v_0 the initial velocity in km s^{-1} , and Z_C is the zenith angle.

396 Note that for the PE criterion to be properly computed, the correct mass scale (as outlined in refs. [35]
397 and [8]) needs to be used (e.g. as given in Table 3.). PE was originally derived using the following luminous
398 efficiency which should always be used for PE computation:

$$\tau = \begin{cases} 1.5 \times 10^{-2.75}, & \text{for } v_0 \leq 9.3 \text{ km s}^{-1} \\ 1.5 \times 10^{-5.60+2.92 \log v_0}, & \text{for } 9.3 < v_0 \leq 12.5 \text{ km s}^{-1} \\ 1.5 \times 10^{-3.24+0.77 \log v_0}, & \text{for } 12.5 < v_0 \leq 17.0 \text{ km s}^{-1} \\ 1.5 \times 10^{-2.50+0.17 \log v_0}, & \text{for } 17.0 < v_0 \leq 27.0 \text{ km s}^{-1} \\ 1.5 \times 10^{-3.69+1.00 \log v_0}, & \text{otherwise} \end{cases} \quad (13)$$

399 where τ is the dimensionless luminous efficiency as a fraction (not percentage), and v_0 the initial velocity in
400 km s^{-1} .

401 These values of luminous efficiency are considered to be underestimated compared to contemporary
402 models. For example, for the Alberta fireball with $v_0 = 62.1 \text{ km s}^{-1}$ the luminous efficiency according to

403 equation 13 is $\tau = 1.9\%$, while in the modelling we used values between 10% and 14% (depending on the
404 mass).

405 **0.9 Meteoroid strength and dynamic pressure**

406 Meteoroid fragmentation is commonly assumed to occur when the dynamic pressure $P_{\text{dyn}} = \Gamma \rho_{\text{air}} v^2$ exceeds
407 the mechanical strength of the body [77]. In most cases, meteorite-dropping fireballs of asteroidal origin
408 fragment in two phases: the first from 0.04–0.12 MPa and the second from 0.9–5 MPa [36]. These are
409 significantly lower than the tensile strengths of ordinary chondrites which survive atmospheric flight and
410 are recovered, which are measured to be between 20 – 40 MPa [9]. Rarely, meteoroids act like monoliths
411 and show no evidence of fragmentation [79], possibly due to a lack of internal cracking which is commonly
412 invoked as the mechanism which causes fragmentation at lower strengths [42]. As we model fragmentation
413 directly and use both the light curve and the dynamics as a constraint, the derived values should be accurate
414 to within $\pm 25\%$, which is the short-term variation in the atmosphere mass density that is not captured by
415 current atmosphere models [48].

416 **0.10 Mass distribution of LPC objects**

417 Figure 14 shows the mass distribution of observed events in the ref. [35] mass scale (about $10\times$ more than
418 estimates using a contemporary value of the luminous efficiency, but appropriate for PE calculations). Due
419 to small-number statistics, it is not possible to determine which theoretical value of the cumulative mass
420 index fits to the data set and thus extend the estimates to other mass ranges. Both $s = 1.67$ (ref. [80]) and
421 $s = 1.83$ (collisional equilibrium, ref. [81]) are plausible.

422 **Code availability**

423 The optical data were calibrated using the open source `SkyFit2` software available in the RMS library at URL
424 <https://github.com/CroatianMeteorNetwork/RMS>.

425 The `WesternMeteorPyLib` (`wmpl`) library was used to compute the trajectory and fit the meteoroid abla-
426 tion model to the observations. It is available at URL <https://github.com/wmpg/WesternMeteorPyLib/>.

427 **Data availability**

428 The trajectory data are included in this article as Supplementary Data files. The raw images are available
429 upon request.

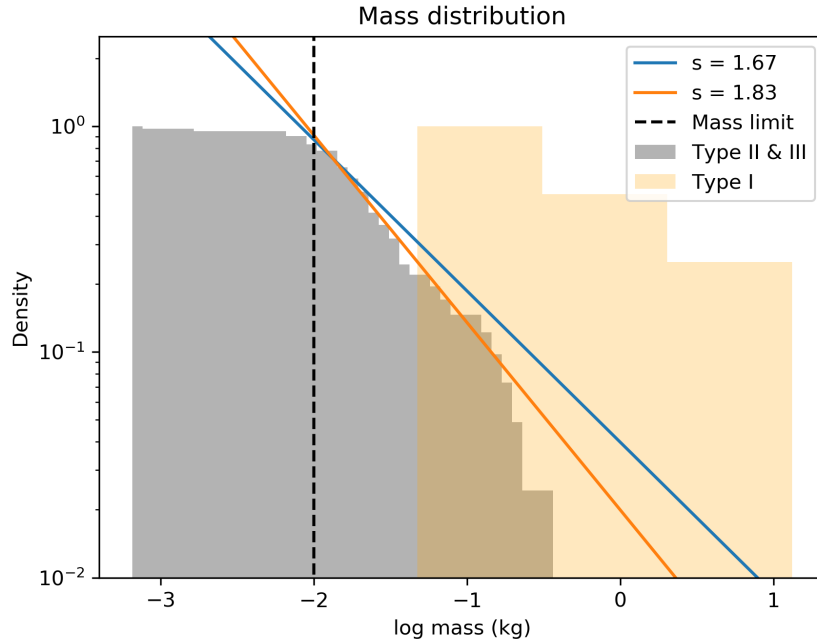


Figure 14: Comparison between the mass distribution of $T_J < 2$ objects used in this work.

References

- [1] Spurný, P., Borovička, J., Mucke, H. & Svoreň, J. Discovery of a new branch of the taurid meteoroid stream as a real source of potentially hazardous bodies. *Astronomy & Astrophysics* **605**, A68 (2017).
- [2] Tóth, J. *et al.* Amos-the slovak worldwide all-sky meteor detection system. In *Proceedings of the 1st NEO and Debris Detection Conference, Darmstadt, Germany* (2019).
- [3] Devillepoix, H. *et al.* A global fireball observatory. *Planetary and Space Science* **191**, 105036 (2020).
- [4] Colas, F. *et al.* Fripon: a worldwide network to track incoming meteoroids. *Astronomy & Astrophysics* **644**, A53 (2020).
- [5] Vida, D. *et al.* The global meteor network - methodology and first results. *Monthly Notices of the Royal Astronomical Society*, submitted (in press).
- [6] Goodman, S. J. *et al.* The goes-r geostationary lightning mapper (glm). *Atmospheric research* **125**, 34–49 (2013).
- [7] Jenniskens, P. *et al.* Detection of meteoroid impacts by the geostationary lightning mapper on the goes-16 satellite. *Meteoritics & Planetary Science* **53**, 2445–2469 (2018).

- 444 [8] Ceplecha, Z. Earth’s influx of different populations of sporadic meteoroids from photographic and
445 television data. *Bulletin of the Astronomical Institutes of Czechoslovakia* **39**, 221–236 (1988).
- 446 [9] Flynn, G. J., Consolmagno, G. J., Brown, P. & Macke, R. J. Physical properties of the stone meteorites:
447 Implications for the properties of their parent bodies. *Geochemistry* **78**, 269–298 (2018).
- 448 [10] Binzel, R. P., Reddy, V. & Dunn, T. The near-earth object population: Connections to comets, main-
449 belt asteroids, and meteorites. *Asteroids IV* **1**, 243 (2015).
- 450 [11] Weissman, P. R., A’Hearn, M. F., McFadden, L. & Rickman, H. Evolution of comets into asteroids.
451 *Asteroids III* **1**, 669 (2002).
- 452 [12] Brownlee, D., Joswiak, D. & Matrajt, G. Overview of the rocky component of wild 2 comet samples:
453 Insight into the early solar system, relationship with meteoritic materials and the differences between
454 comets and asteroids. *Meteoritics & Planetary Science* **47**, 453–470 (2012).
- 455 [13] Weissman, P. R. & Levison, H. F. Origin and evolution of the unusual object 1996 pw: Asteroids from
456 the oort cloud? *The Astrophysical Journal Letters* **488**, L133 (1997).
- 457 [14] Shannon, A., Jackson, A. P., Veras, D. & Wyatt, M. Eight billion asteroids in the oort cloud. *Monthly*
458 *Notices of the Royal Astronomical Society* **446**, 2059–2064 (2015).
- 459 [15] Meech, K. J. *et al.* Inner solar system material discovered in the oort cloud. *Science Advances* **2**,
460 e1600038 (2016).
- 461 [16] Walsh, K. J., Morbidelli, A., Raymond, S. N., O’Brien, D. P. & Mandell, A. M. A low mass for mars
462 from jupiter’s early gas-driven migration. *Nature* **475**, 206–209 (2011).
- 463 [17] Izidoro, A., de Souza Torres, K., Winter, O. & Haghighipour, N. A compound model for the origin of
464 earth’s water. *The Astrophysical Journal* **767**, 54 (2013).
- 465 [18] Zwart, S. P. Oort cloud ecology-i. extra-solar oort clouds and the origin of asteroidal interlopers.
466 *Astronomy & Astrophysics* **647**, A136 (2021).
- 467 [19] Bottke Jr, W. F. *et al.* The fossilized size distribution of the main asteroid belt. *Icarus* **175**, 111–140
468 (2005).
- 469 [20] Minton, D. A. & Malhotra, R. Dynamical erosion of the asteroid belt and implications for large impacts
470 in the inner solar system. *Icarus* **207**, 744–757 (2010).
- 471 [21] Clement, M. S., Raymond, S. N. & Kaib, N. A. Excitation and depletion of the asteroid belt in the
472 early instability scenario. *The Astronomical Journal* **157**, 38 (2019).

- 473 [22] de Sousa Ribeiro, R. *et al.* Dynamical evidence for an early giant planet instability. *Icarus* **339**, 113605
474 (2020).
- 475 [23] Marrocchi, Y., Delbo, M. & Gounelle, M. The astrophysical context of collision processes in meteorites.
476 *Meteoritics & Planetary Science* (2021).
- 477 [24] Morbidelli, A. & Raymond, S. N. Challenges in planet formation. *Journal of Geophysical Research:*
478 *Planets* **121**, 1962–1980 (2016).
- 479 [25] Johansen, A. *et al.* Rapid planetesimal formation in turbulent circumstellar disks. *Nature* **448**, 1022–
480 1025 (2007).
- 481 [26] Levison, H. F., Kretke, K. A. & Duncan, M. J. Growing the gas-giant planets by the gradual accumu-
482 lation of pebbles. *Nature* **524**, 322–324 (2015).
- 483 [27] Brož, M., Chrenko, O., Nesvorný, D. & Dauphas, N. Early terrestrial planet formation by torque-driven
484 convergent migration of planetary embryos. *Nature Astronomy* 1–5 (2021).
- 485 [28] DeSouza, S. R., Roig, F. & Nesvorný, D. Can a jumping-jupiter trigger the moon’s formation impact?
486 *arXiv preprint arXiv:2107.04181* (2021).
- 487 [29] Hicks, M., Buratti, B., Newburn Jr, R. & Rabinowitz, D. Physical observations of 1996 pw and 1997
488 se5: Extinct comets or d-type asteroids? *Icarus* **143**, 354–359 (2000).
- 489 [30] Boe, B. *et al.* The orbit and size-frequency distribution of long period comets observed by pan-starrs1.
490 *Icarus* **333**, 252–272 (2019).
- 491 [31] Davidsson, B. *et al.* The primordial nucleus of comet 67p/churyumov-gerasimenko. *Astronomy &*
492 *Astrophysics* **592**, A63 (2016).
- 493 [32] Boe, B. *et al.* Distinguishing between solar system formation models with manxes (or maybe not). In
494 *EPSC-DPS Joint Meeting 2019*, vol. 2019, EPSC–DPS2019 (2019).
- 495 [33] Binzel, R. P. *et al.* Observed spectral properties of near-earth objects: results for population distribution,
496 source regions, and space weathering processes. *Icarus* **170**, 259–294 (2004).
- 497 [34] Kaluna, H. M., Masiero, J. R. & Meech, K. J. Space weathering trends among carbonaceous asteroids.
498 *Icarus* **264**, 62–71 (2016).
- 499 [35] Ceplecha, Z. & McCrosky, R. Fireball end heights: A diagnostic for the structure of meteoric material.
500 *Journal of Geophysical Research* **81**, 6257–6275 (1976).

- 501 [36] Borovička, J., Spurný, P. & Šrbený, L. Two strengths of ordinary chondritic meteoroids as derived
502 from their atmospheric fragmentation modeling. *The Astronomical Journal* **160**, 42 (2020).
- 503 [37] Brown, P., Spalding, R., ReVelle, D. O., Tagliaferri, E. & Worden, S. The flux of small near-earth
504 objects colliding with the earth. *Nature* **420**, 294–296 (2002).
- 505 [38] Borovička, J., Spurný, P. & Koteš, P. Atmospheric deceleration and light curves of draconid meteors
506 and implications for the structure of cometary dust. *Astronomy & Astrophysics* **473**, 661–672 (2007).
- 507 [39] Vojáček, V., Borovička, J., Koteš, P., Spurný, P. & Štork, R. Properties of small meteoroids studied
508 by meteor video observations. *Astronomy & Astrophysics* **621**, A68 (2019).
- 509 [40] Hornung, K. *et al.* A first assessment of the strength of cometary particles collected in-situ by the
510 cosima instrument onboard rosetta. *Planetary and Space Science* **133**, 63–75 (2016).
- 511 [41] Borovička, J. *et al.* The košice meteorite fall: Atmospheric trajectory, fragmentation, and orbit. *Meteo-*
512 *oritics & Planetary Science* **48**, 1757–1779 (2013).
- 513 [42] Borovička, J. Physical and chemical properties of meteoroids as deduced from observations. *Proceedings*
514 *of the International Astronomical Union* **1**, 249–271 (2005).
- 515 [43] Ceplecha, Z. *et al.* Meteor phenomena and bodies. *Space Science Reviews* **84**, 327–471 (1998).
- 516 [44] Borovička, J., Popova, O., Nemtchinov, I., Spurný, P. & Ceplecha, Z. Bolides produced by impacts of
517 large meteoroids into the earth’s atmosphere: comparison of theory with observations. i. benesov bolide
518 dynamics and fragmentation. *Astronomy and Astrophysics* **334**, 713–728 (1998).
- 519 [45] Brownlee, D. *et al.* Comet 81p/wild 2 under a microscope. *science* **314**, 1711–1716 (2006).
- 520 [46] Kimura, H. *et al.* The tensile strength of dust aggregates consisting of small elastic grains: constraints
521 on the size of condensates in protoplanetary discs. *Monthly Notices of the Royal Astronomical Society*
522 **496**, 1667–1682 (2020).
- 523 [47] Biele, J. *et al.* The landing (s) of philae and inferences about comet surface mechanical properties.
524 *Science* **349** (2015).
- 525 [48] Vida, D. *et al.* High precision meteor observations with the canadian automated meteor observatory:
526 Data reduction pipeline and application to meteoroid mechanical strength measurements. *Icarus* **354**,
527 114097 (2021).
- 528 [49] Thomas, H., Ratke, L. & Kochan, H. Crushing strength of porous ice-mineral bodies-relevance for
529 comets. *Advances in Space Research* **14**, 207–216 (1994).

- 530 [50] Spohn, T. *et al.* Thermal and mechanical properties of the near-surface layers of comet 67p/churyumov-
531 gerasimenko. *Science* **349** (2015).
- 532 [51] Strazzulla, G., Baratta, G., Johnson, R. & Donn, B. Primordial comet mantle: irradiation production
533 of a stable organic crust. *Icarus* **91**, 101–104 (1991).
- 534 [52] Kömle, N. I. *et al.* Impact penetrometry on a comet nucleus—interpretation of laboratory data using
535 penetration models. *Planetary and space Science* **49**, 575–598 (2001).
- 536 [53] Matlovič, P., Tóth, J., Rudawska, R. & Kornoš, L. Spectra and physical properties of taurid meteoroids.
537 *Planetary and Space Science* **143**, 104–115 (2017).
- 538 [54] Borovička, J. & Spurný, P. Physical properties of taurid meteoroids of various sizes. *Planetary and*
539 *Space Science* **182**, 104849 (2020).
- 540 [55] Borovička, J. & Jenniskens, P. Time resolved spectroscopy of a leonid fireball afterglow. *Earth, Moon,*
541 *and Planets* **82**, 399–428 (2000).
- 542 [56] Spurný, P. & Borovička, J. En010697 karlstejn: the first type i fireball on retrograde orbit. In *Meteoroids*
543 *1998*, 143 (1999).
- 544 [57] Spurný, P. & Borovička, J. Detection of a high density meteoroid on cometary orbit. In *IAU Colloq.*
545 *173: Evolution and Source Regions of Asteroids and Comets*, 163 (1999).
- 546 [58] Kokhirova, G. & Borovička, J. Observations of the 2009 leonid activity by the tajikistan fireball network.
547 *Astronomy & Astrophysics* **533**, A115 (2011).
- 548 [59] Borovička, J. *et al.* *Physical and Chemical Properties of Meteoroids*, 37 (Cambridge University Press,
549 2019).
- 550 [60] Revelle, D. O. & Ceplecha, Z. Bolide physical theory with application to PN and EN fireballs. In
551 Warmbein, B. (ed.) *Meteoroids 2001 Conference*, vol. 495 of *ESA Special Publication*, 507–512 (2001).
- 552 [61] Halliday, I., Griffin, A. A. & Blackwell, A. T. Detailed data for 259 fireballs from the canadian camera
553 network and inferences concerning the influx of large meteoroids. *Meteoritics & Planetary Science* **31**,
554 185–217 (1996).
- 555 [62] Spurný, P. Recent fireballs photographed in central europe. *Planetary and Space Science* **42**, 157–162
556 (1994).
- 557 [63] Spurný, P. Exceptional fireballs photographed in central europe during the period 1993–1996. *Planetary*
558 *and space science* **45**, 541–555 (1997).

- 559 [64] Brown, P., Wiegert, P., Clark, D. & Tagliaferri, E. Orbital and physical characteristics of meter-scale
560 impactors from airburst observations. *Icarus* **266**, 96–111 (2016).
- 561 [65] Levison, H. F., Duncan, M. J., Brassier, R. & Kaufmann, D. E. Capture of the sun’s oort cloud from
562 stars in its birth cluster. *Science* **329**, 187–190 (2010).
- 563 [66] Howie, R. M. *et al.* Submillisecond fireball timing using de bruijn timecodes. *Meteoritics & Planetary
564 Science* **52**, 1669–1682 (2017).
- 565 [67] Vida, D., Gural, P. S., Brown, P. G., Campbell-Brown, M. & Wiegert, P. Estimating trajectories of
566 meteors: an observational monte carlo approach–i. theory. *Monthly Notices of the Royal Astronomical
567 Society* **491**, 2688–2705 (2020).
- 568 [68] Vida, D., Brown, P. G., Campbell-Brown, M., Wiegert, P. & Gural, P. S. Estimating trajectories of
569 meteors: an observational monte carlo approach–ii. results. *Monthly Notices of the Royal Astronomical
570 Society* **491**, 3996–4011 (2020).
- 571 [69] Subasinghe, D., Campbell-Brown, M. & Stokan, E. Luminous efficiency estimates of meteors-i. uncer-
572 tainty analysis. *Planetary and Space Science* **143**, 71–77 (2017).
- 573 [70] Spurný, P. *et al.* Analysis of instrumental observations of the jesenice meteorite fall on april 9, 2009.
574 *Meteoritics & Planetary Science* **45**, 1392–1407 (2010).
- 575 [71] Šegon, D., Vukić, M., Šegon, M., Andreić, v. & Gural, P. S. Meteors in the near-infrared as seen in
576 the ondrejov catalogue of representative meteor spectra. In *Proceedings of the International Meteor
577 Conference*, 107–108 (2018).
- 578 [72] Cooke, W. J. & Moser, D. E. The status of the nasa all sky fireball network. In *Proceedings of the
579 International Meteor Conference, edited by: Gyssens, M. and Roggemans, P., IMO*, vol. 912, 1518
580 (2011).
- 581 [73] Borovička, J. *et al.* The instrumentally recorded fall of the križevci meteorite, croatia, february 4, 2011.
582 *Meteoritics & Planetary Science* **50**, 1244–1259 (2015).
- 583 [74] Borovička, J., Spurný, P., Grigore, V. I. & Svoreň, J. The january 7, 2015, superbolide over romania
584 and structural diversity of meter-sized asteroids. *Planetary and Space Science* **143**, 147–158 (2017).
- 585 [75] Borovička, J., Popova, O. & Spurný, P. The maribo cm 2 meteorite fall—survival of weak material at
586 high entry speed. *Meteoritics & Planetary Science* **54**, 1024–1041 (2019).
- 587 [76] Picone, J., Hedin, A., Drob, D. P. & Aikin, A. Nrlmsise-00 empirical model of the atmosphere: Statistical
588 comparisons and scientific issues. *Journal of Geophysical Research: Space Physics* **107**, SIA–15 (2002).

- 589 [77] Popova, O., Borovicka, J. & Campbell-Brown, M. Modelling the entry of meteoroids. *Meteoroids:*
590 *Sources of Meteors on Earth and Beyond* **25**, 9 (2019).
- 591 [78] Weryk, R. J. & Brown, P. G. Simultaneous radar and video meteors—ii: Photometry and ionisation.
592 *Planetary and Space Science* **81**, 32–47 (2013).
- 593 [79] Borovička, J. & Spurný, P. The carancas meteorite impact–encounter with a monolithic meteoroid.
594 *Astronomy & Astrophysics* **485**, L1–L4 (2008).
- 595 [80] Brassier, R. A two-stage formation process for the oort comet cloud and its implications. *Astronomy &*
596 *Astrophysics* **492**, 251–255 (2008).
- 597 [81] Durda, D. D. & Dermott, S. F. The collisional evolution of the asteroid belt and its contribution to the
598 zodiacal cloud. *Icarus* **130**, 140–164 (1997).

599 **End Notes**

600 **Acknowledgements**

601 We thank Mr. Robert Howell for first bringing this fireball to our attention and Mr. Airell DesLauriers for
602 providing raw footage from his security camera in Cochrane, AB. Funding for this work was provided in part
603 through NASA co-operative agreement 80NSSC21M0073, by the Natural Sciences and Engineering Research
604 Council of Canada Discovery Grants program (Grants no. RGPIN-2016-04433 & RGPIN-2018-05659), the
605 Canada Research Chairs program, the Slovak Research and Development Agency grant APVV-16-0148, and
606 the Slovak Grant Agency for Science grant VEGA 01/0596/18.

607 **Author Contributions**

608 DV coordinated the effort, performed the analysis, implemented the software, and wrote the manuscript.
609 PGB initially coordinated the effort and provided scientific insight. HD computed an initial trajectory
610 and provided the raw GFO data. PW made valuable scientific interpretations of the results and added a
611 connection to recent comet discoveries, and performed the orbital integrations. DEM helped put together
612 the source of MORP, PN, and EN data, systematically collected and organized all casual recordings of the
613 fireball, provided the GLM observations, and identified fireballs for GLM calibration. PM and JT provided
614 observations of a fireball jointly observed with the AMOS system and GLM. CDKH and PJAH provided the
615 GFO data from the Miquelon Lake and Vermilion cameras and helped contact the local people who observed
616 the fireball. WJC provided initial coordination. DWH provided the GoPro video and took DSLR images for
617 its photometric calibration.

618 **Declaration of Interests**

619 The authors declare no competing interests.

Supplementary Files

This is a list of supplementary files associated with this preprint. Click to download.

- [NATASTRON21064378Asupplementary.zip](#)